JOURNAL OF THERMOPHYSICS AND HEAT TRANSFER
Vol. 11, No. 2, April–June 1997

Convective and Radiative Coupling in a Burner-Supported Diffusion Flame

O. A. Ezekoye* and Z. Zhang†
University of Texas at Austin, Austin, Texas 78712

A computational investigation of the influences of convective and radiative coupling on the total radiative transfer and burner characteristics for a burner-supported diffusion flame are carried out. By coupling the soot and gas phase chemistry with radiative heat transfer processes, detailed effects of radiation from both the soot and gas phase species on the flame dynamics can be examined in a transient microgravity spherical acetylene–air diffusion flame. The gas phase reaction is modeled by one-step chemical kinetics. The soot reaction mechanism includes nucleation, surface growth, oxidation, and coagulation steps. The radiation from both soot and the gas phase species are calculated by employing a spherical harmonics (P-1 approximation) model. The local Planck mean absorption coefficients of the radiatively participating species are specified in the computations. Unlike normal gravity acetylene–air steady-state jet diffusion flames in which the radiative emission from soot is significantly larger than from gas species, it is found that for a microgravity diffusion flame, except at very early times, the radiation from the gas products exceeds soot radiation.

Nomenclature

A = pre-exponential constants in reaction rate expressions
A_s = soot surface area per unit volume
a, b, c, d = exponent constants in the reaction rate expressions
a_p = Planck mean absorption
B = temperature-dependent constant in reaction rate expression
C_a = agglomeration rate constant
$C_{\min}$ = number of carbon atoms in the incipient carbon particle
C_2 = Planck's second constant
c_p = specific heat
D_{im} = diffusion coefficient of species i relative to mixture
E = activation energy
f_v = soot volume fraction
G = irradiation
h = total enthalpy
h_f^0 = heat of formation
k = constant, Arrhenius reaction rate
N_A = Avogadros' number
N_c = soot particle number density
q_r = radiative heat flux
R = universal gas constant, radius of combustor
r = radial coordinate, reaction rates associated with soot reaction
S = source term in the conservation equation
T = temperature
t = time
u = velocity
$\dot{V}$ = volumetric flow rate
V_i = diffusion velocity of species i
W = molecular weight
Y = mass fraction
$\boldsymbol{\beta}$ = agglomeration kernel
ζ = fuel-dependent radiative constant
$\boldsymbol{\lambda}$ = thermal conductivity
μ = dynamic viscosity
ρ = density
σ = Stefan–Boltzmann constant
$\dot{\omega}$ = reaction rate

Subscripts
c = associated with soot
F = fuel
g = gas
i = ith species
t = total
th = thermophoretic
0 = standard state

Introduction

NONPREMIXED flames are used in a range of technologies in which their radiative heat transfer characteristics are of great importance. A difficulty in simulating these flames is the required coupling between the condensed phase (soot) and gas phase chemical kinetics when considering the effects of radiative thermal transport. Most previous studies on sooting diffusion flames related the soot reaction rates to a conserved scalar, the mixture fraction. The gas phase concentrations as well as temperature were then typically interpolated from a property map, which exclusively relies on experimental measurements for individual flame configurations.[1–5] Radiative transport was often incorporated into the energy equation by modifying the sources in the energy equation with a radiation loss fraction.[6] In a study by Sivathanu and Gore,[7] the radiation effects on soot kinetics in a laminar acetylene/air diffusion flames were studied. A gas phase mixture fraction equation is solved together with the energy equation where the gas phase mass fractions are interpolated from the state relationships. The gas phase kinetics and soot kinetics were therefore decoupled and thermal effects associated with radiative cooling were incapable of modifying the gas phase species evolution. In recent work by Ezekoye and Zhang[8] the implications of the underlying assumptions within soot formation and oxidation models were investigated; the gas phase mass fraction equations, soot

---

Received May 10, 1996; revision received Aug. 24, 1996; accepted for publication Sept. 24, 1996.

*Assistant Professor of Mechanical Engineering, Department of Mechanical Engineering.

†Graduate Research Assistant, Department of Mechanical Engineering.

mass fraction, and number density equation and energy equation with radiation effects were solved in a fully coupled manner. The flame geometry that was simulated in that study was a microgravity diffusion flame where measurements had been made by Atreya et al.[9] In Ref. 8 effects of OH oxidation on the soot distribution as well as effects of the soot agglomeration model were discussed in detail. That study is typical of sooting flame computational studies where the emphasis has been on the description of the soot chemistry models. Relatively few studies consider the effects of the heat transfer processes on modifications to the flame structure.

In the present study, a more detailed analysis is made of the burner previously characterized by Atreya et al.[9] As with the previous study,[8] this study numerically investigates the effects of radiation from both the soot and the gas phase on the soot kinetics in a transient microgravity spherical acetylene/air diffusion flame by fully coupling the soot, gas phase chemistry, and radiation. The gas phase reaction is modeled by a single-step reaction, and the soot reaction mechanism includes nucleation, surface growth, oxidation, and coagulation steps.[6,10] The radiation from both soot and the gas phase are considered and calculated by employing a spherical harmonics (P-1 approximation) model. Unlike the previous study where the heat transfer processes were not investigated in detail, this study more rigorously treats the heat transfer coupling. As an example, in Ref. 8 a constant Planck mean absorption coefficient was used for the gas phase species, whereas in this study, the Planck mean absorption coefficients of all gas phase products are specified as functions of temperature and local gas concentration.[11] The use of more detailed radiative transfer properties affects the prescription of the soot chemistry (in particular, the soot oxidation rates). Further, more detailed flow and heat transfer characteristics of the burner are discussed within this study and interesting couplings between the convective and radiative transfer to the burner are noted.

Theory

Governing Equations

In the experiments of Atreya et al.[9] a porous spherical burner was used to produce a low strain rate spherical diffusion flame in a microgravity environment. The experimental system is modeled in this study by formulating a one-dimensional, unsteady diffusion flame in spherical coordinates. The equations governing the combustion process are the following:

Mass conservation equation

$$\frac{\partial(\rho_t r^2)}{\partial t} + \frac{\partial(\rho_t u r^2)}{\partial r} = 0 \tag{1}$$

Gas phase species conservation equation

$$\rho_t r^2 \left(\frac{\partial Y_i}{\partial t} + u\,\frac{\partial Y_i}{\partial r}\right) = \dot{\omega}_i r^2 - \frac{\partial}{\partial r}\,(\rho_t Y_i V_i r^2) \tag{2}$$

Gas phase energy conservation equation

$$\begin{aligned}\rho_t c_p r^2 \left(\frac{\partial T}{\partial t} + u\,\frac{\partial T}{\partial r}\right) &= \frac{\partial}{\partial r}\left[r^2\left(\boldsymbol{\lambda}\,\frac{\partial T}{\partial r} - q_r\right)\right] - r^2 \sum_{i=1}^{K} \dot{\omega}_i h_i \\ &\quad - \rho_t r^2 \sum_{i=1}^{K} Y_i c_{pi} V_i\,\frac{\partial T}{\partial r} + (-S_{cf0} h^0_{f,F} + S_{c0x} h^0_{f,c0}) r^2\end{aligned} \tag{3}$$

Soot mass fraction conservation equation

$$r^2 \rho_t \left(\frac{\partial Y_c}{\partial t} + u\,\frac{\partial Y_c}{\partial r}\right) = \frac{\partial}{\partial r}\left[r^2\left(\frac{\mu}{Sc}\,\frac{\partial Y_c}{\partial r} - \rho_t u_{\mathrm{th}} Y_c\right)\right] + r^2 S_{Y_c} \tag{4}$$

Soot particle number density equation

$$r^2 \rho_t \left(\frac{\partial N_c}{\partial t} + u\,\frac{\partial N_c}{\partial r}\right) = \frac{\partial}{\partial r}\left[r^2\left(\frac{\mu}{Sc}\,\frac{\partial N_c}{\partial r} - \rho_t u_{\mathrm{th}} N_c\right)\right] + r^2 S_{N_c} \tag{5}$$

where the total enthalpy of species i is

$$h_i = h^0_{fi} + \int_{T_0}^{T} c_{pi}\,\mathrm{d}T \tag{6}$$

The fourth term in the right-hand side of the energy equation approximates the enthalpy transfer during the phase change process.[7] Sc is the Schmidt number of the soot species and is specified to be 1000. The Schmidt number is approximately 1000 for spherical aerosol particles with a diameter of approximately 20 nm.[12] Although the soot particles in this study are larger than 20 nm, it is found that the numerical scheme utilized (power law treatment of convective terms) introduces numerical diffusion of the same order as the Schmidt number of 1000. Thus, specifying larger values of the Schmidt number would not affect the perceived diffusion of the soot species. All thermodynamic properties such as species total enthalpy, species specific heat capacity, gas phase mixture density (which obeys the ideal gas law), are evaluated from CHEMKIN-II.[13] The transport properties such as species diffusion coefficient, diffusion velocity, mixture thermal conductivity, mixture dynamic viscosity are evaluated from a gas-phase multicomponent transport properties package.[14]

For soot mass fraction and soot particle number density equations, the velocity includes a thermophoretic component.[15]

Initial and Boundary Conditions

A fuel stream exits from a spherical porous burner of radius 1.09 cm surrounded by quiescent air. The fuel mass flow rate is maintained at 20 cm^3/s. The initial mixture fraction profile is assumed to be in the form of complimentary error function, with the mixture fraction specified to be unity at the burner surface, and the stoichiometric value at $r = 1.4$ cm, which is taken from the experimental results, to be the initial flame location. The calculation domain is from $r = 1.09$ to 9.09 cm. The profiles of major species mass fraction and temperature at the initial time are interpolated as functions of mixture fraction from the experimental data of Skinner[16] and Gore and Skinner.[17] The boundary conditions at the sphere surface are

$$\frac{\dot{V}\rho_{f\infty}}{A} = \rho u\big|_{r=R} \tag{7}$$

$$\frac{\dot{V}\rho_{f\infty}}{A}\,(Y_{F\infty} - Y_{FR}) = -\rho D_{Fm}\,\frac{\partial Y_F}{\partial r}\bigg|_{r=R} \tag{8}$$

$$\frac{\dot{V}\rho_{f\infty}}{A}\,(h_\infty - h_R) = -\boldsymbol{\lambda}\,\frac{\partial T}{\partial r}\bigg|_{r=R} + q_r\big|_{r=R} + \rho \sum_{i=1}^{N} h_i D_{im}\,\frac{\partial Y_i}{\partial r}\bigg|_{r=R} \tag{9}$$

The boundary conditions at $r = 9.09$ cm are zero flux for all dependent variables.

Solution Procedure

The conservation equations are solved by a control volume finite difference scheme. The velocity is obtained from the conservation of mass equation. All of the thermodynamic properties are obtained from the CHEMKIN-II package.[13] The transport properties are calculated from the multicomponent transport properties package.[14] The total density (gas phase and soot) is obtained by a local homogeneity assumption.[18] The species mass fraction equations, soot mass fraction conservation equation, soot number density conservation equation,

equation of state, and energy equation are solved iteratively at each time step. Continuity is satisfied by requiring that the summation of all species mass fractions including soot be equal to unity. To obtain a converged solution, an adaptive time-stepping routine based on the peak reaction rate magnitude is used. The convergence criterion is satisfied by restricting the relative errors of all independent variables to be less than 10^{-3} for each time step. Two criteria were used to evaluate the grid resolution. First, it was imperative that the grid be fine enough to resolve the reaction zone thickness. Second, the effects of additional grid refinement were determined by reducing the mesh size from 0.02 to 0.016 cm, resulting in less than 1% difference between the two solutions. All calculations were then made using the 0.02-cm mesh size.

Soot Kinetics

The soot kinetics mechanism includes soot nucleation, surface growth, oxidation, and particle coagulation steps.[6,10] The soot reaction rate terms of Fairweather et al.[10] are employed in this work. The rate constants are not included here and can be found in Ref. 10.

The sources in the soot mass fraction include the nucleation, surface growth, and O_2 oxidation rate terms, respectively,

$$S_{Y_c} = k_i[C_2H_2]W_c + k_{ii}A_s[C_2H_2]W_c - k_{iii}A_s[O_2] \tag{10}$$

where A_s is

$$A_s = \pi^{1/3}6^{2/3}f_v^{2/3}(\rho N_c)^{1/3}$$

It should be noted that as in Ref. 10 the number concentration is defined to be number of particles per mass of mixture. The sources in the soot number density equation include the nucleation and agglomeration rate terms

$$S_{N_c} = (2/C_{\min})N_Ak_i[C_2H_2] - \beta\rho_t^2W_c^{-1/6}Y_c^{1/6}N_c^{11/6} \tag{11}$$

where

$$\beta = 2C_a[6W_c/\pi\rho_{c(s)}]^{1/6}[6kT/\rho_{c(s)}]^{1/2}$$

is the agglomeration kernel. The soot kinetics rates and associated constants from Fairweather et al.[10] are used without modification in this study. In that study, the number of carbon atoms in the incipient carbon particle $C_{\min}$ is specified to be 9 $\times 10^{+4}$, and as a result the incipient carbon particles have radii of 60 nm. C_a is 3.0, N_A is 6.022 $\times 10^{+26}$ particles kmol^{-1}, k is 1.381 $\times 10^{-23}$ JK^{-1}, ρ_c is 2000 kg m^{-3}, and W_c is 12 kg kmol^{-1}.

A single-step reaction mechanism for acetylene/air flame of Westbrook and Dryer[19] was employed in this study.

Radiation Model

Several comparisons are available in the literature showing the accuracy of the P1 approximation against higher level approximations. The P1 deviates most at extreme values of the optical thickness (maximum deviations of 20%) and is quite accurate otherwise.[11] For the most part, the flame that we simulate has an optical thickness close to unity where the P1 is not such a poor approximation. For a pure radiation problem errors in the heat flux of order 10% are often undesirable, but for a combustion problem where radiative transfer may influence temperatures by approximately 30%, the errors in the radiative transfer model of order 10% only contribute to 3% errors in the overall combustion dynamics and are acceptable.

For nonscattering conditions, the governing equation for the P1 or differential approximation reduces to the form

$$\nabla_\tau^2 G = 3(G - 4\sigma T^4) \tag{12}$$

where τ is the optical depth. The net radiation flux is related to the irradiation by

$$\bar{\boldsymbol{q}}_r = -\tfrac{1}{3}\boldsymbol{\nabla}_\tau G \tag{13}$$

The boundary condition for G equation is given by

$$-[(2 - \varepsilon)/\varepsilon]\tfrac{2}{3}\hat{n}\cdot\boldsymbol{\nabla}_\tau G + G = 4\sigma T_{bw} \tag{14}$$

where T_{bw} and ε are the temperature and the emissivity at the boundary, respectively. The Planck mean absorption coefficient of the soot species can be shown to be

$$a_{p,s} = 4\zeta f_vT/C_2 \tag{15}$$

where ζ is a fuel-dependent constant, C_2 is Planck's second constant, σ is a Stefan–Boltzmann constant,[20] and f_v is the soot volume fraction. The mean absorption coefficient of each gas species, $a_{p,g}$ is determined from experimental Planck mean absorption coefficient data as a function of temperature and partial pressure.[11] The total extinction coefficient is then given by

$$a_p = a_{p,s} + a_{p,g} \tag{16}$$

Results and Discussion

The microgravity burner of Atreya et al.[9] provides an interesting low strain rate diffusion flame configuration to investigate the interaction of soot chemistry and heat transfer processes. The baseline condition that is investigated corresponds to a fuel flow rate of 20 cc/s and a burner emissivity of unity. For all cases, the spherical geometry allows the flame to self-stabilize toward low strain conditions. Figure 1 shows the scalar dissipation rate, $\chi = 2D|\nabla Z|^2$, in mixture fraction space at three different times. At the earliest time ($t = 0.001$ s), χ is of order 20 s^{-1}, which corresponds to a relatively high strain rate condition. Much in the same way that a lifted jet flame seeks values of the scalar dissipation below the extinction value, the reaction zone in the spherical burner also relaxes toward lower values of the strain rate. Eventually, χ at the flame sheet becomes order unity and the flame trajectory in physical space is shown to become quasisteady. Scalar dissipation values for various flamelets are specified in Peters,[21] and a recent theoretical paper of Chan et al.[22] examined methane flamelets over a range of scalar dissipation rates to show radiation effects on flame structure. Velocity profiles are shown in Fig. 2. At the earliest time shown, there is chemical heat release-induced flame expansion. An interesting and somewhat counter-intuitive effect is shown in the velocity profiles. The velocity is computed from conservation of mass given the low Mach

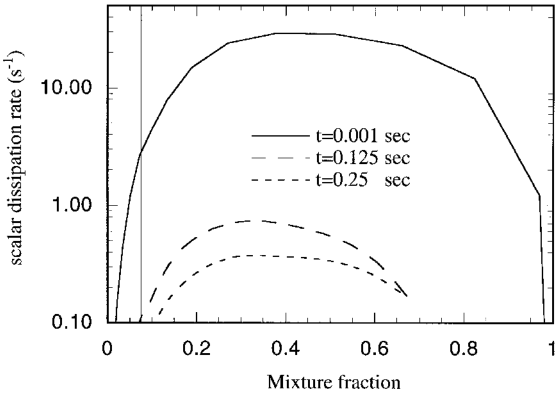

Fig. 1 Scalar dissipation rates are presented in mixture fraction space at different times. Stoichiometric mixture fraction value is approximately 0.07. Fuel flow rate is 20 cc/s and burner emissivity is unity (baseline condition).

number approximation. As a consequence of the phase change process (fuel conversion to soot) and the radiative cooling, the velocity actually reverses. This negative velocity seen at t = 0.001 and 0.125 s is a direct result of the combined effects of rapid density increases (associated with soot formation) and the radiative cooling. For the t = 0.125-s case it is also observed that radiative heating in the postflame gases serves as a source that increases the expansion velocity. The velocity structure observed in this geometry has quite interesting features that require further experimental confirmation.

As a benchmark for these calculations, Fig. 3 shows the computational soot mass as a function of time as compared with experimental data. It is noted that the model of Fairweather et al.[10] underpredicts the soot mass by approximately 25% at the peak soot value. In the case that is shown, the soot model parameters have not been adjusted. This result is different from that presented in our previous work.[8] In that study the gas Planck mean absorption coefficients were taken to be a constant value, and although the soot average temperature profiles were reasonably well predicted (within 20% of the experimental values), the soot mass could not be predicted as well without the addition of an OH oxidation mechanism to the soot kinetics. In the present study it was found that addition of the OH oxidation step does not significantly modify the soot oxidation process. This effect is a result of the improved temperature predictions (within 5% of experimental results), which are associated with the use of more detailed radiative property data. The implication of this effect is that the influence of radiation modification on the temperature and thus soot kinetics can be significant. It was also noted in Ref. 8 that an inherent assumption of the Fairweather et al.[10] soot kinetic mechanism is that the soot species aggregate/coagulate into volume effective spheres. This assumption leads to a low soot specific surface area prediction. In Fig. 3 we contrast the predicted soot mass time history by assuming volume effective agglomeration and then by assuming no agglomeration at all. It is not surprising that the prediction based on the nonagglomerating assumption overpredicts the soot net growth rate. The finite connection area between soot primary particles ensures that the actual soot surface area is between these two limiting assumptions.

Figure 4 shows the calculated flame radius (defined by the maximum temperature) and experimental measurements by Atreya et al.[9] Although the overall shape of the two curves is similar, there is a nearly constant bias between the computed maximum temperature and the experimentally specified flame radius. This disagreement is attributed both to the necessary computational assumptions required to specify an experimentally observed flame radius and also to the difficulties in simulating the experimental ignition procedure. In the experimental study, the flame is ignited at normal gravity (1*g*) conditions by hydrogen prior to the drop package being released (i.e., before μg conditions). In the simulations, an initial mixture fraction profile is assumed by matching the stoichiometric mixture fraction location to the initial experimentally reported flame location at the beginning of microgravity conditions.

The gas species and soot Planck mean absorption coefficients are shown in Fig. 5. Except at earlier times, product gases mean absorption coefficients are larger and more widely distributed in space than soot mean absorption coefficients. This is a very important result. The soot radiation is actually less significant than the gas radiation for much of the computational/experimental time. To show this more clearly, the CO_2 and H_2O mass fraction profiles at various times in the spatial coordinate are presented in Figs. 6 and 7, respectively. Combining these figures with Fig. 8, which shows the temperature distribution, it is concluded that in the microgravity diffusion flame, radiation from the product and fuel species dominates the total radiative output. With increasing time after ignition, hot unburned fuel and products accumulate in phys-

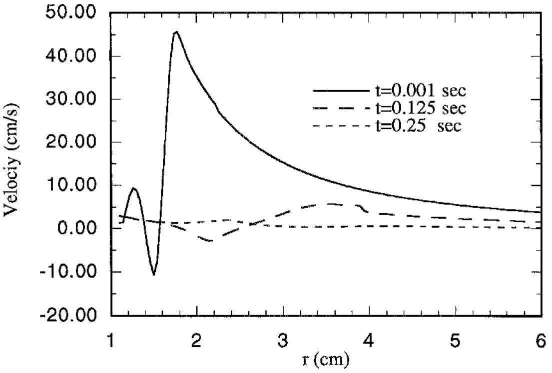

Fig. 2 Velocity profiles at different times are shown in physical space for baseline condition.

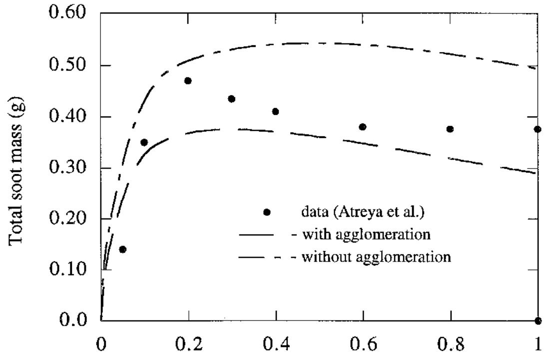

Fig. 3 Computationally predicted soot total mass time history is compared with experimental results from Atreya et al.[9]: $\dot{V}$ = 20 cc/s and ε = 1.

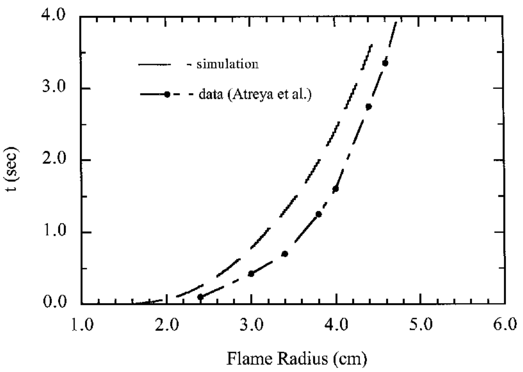

Fig. 4 Flame sheet location based on maximum temperature is compared with experimental results: $\dot{V}$ = 20 cc/s and ε = 1.

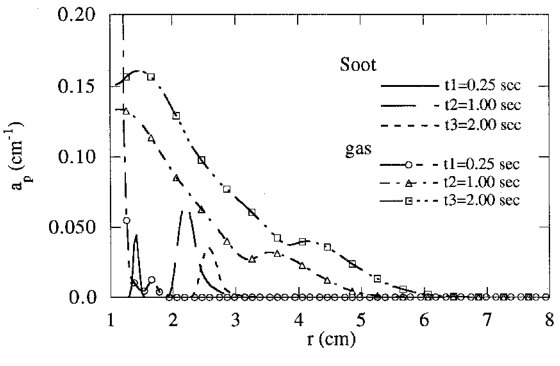

Fig. 5 Spatial distribution of gas (symbols) and soot (no symbols) Planck mean absorption coefficients are presented at different times for baseline condition.

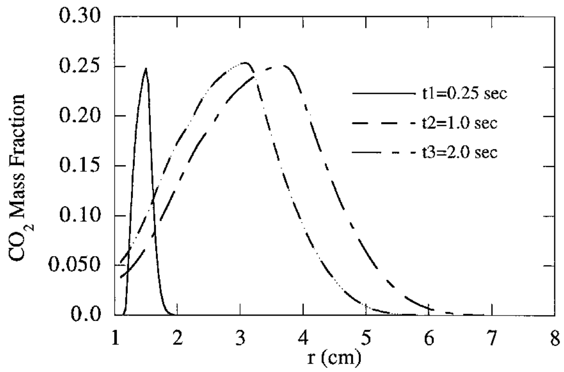

Fig. 6 Calculated CO_2 species profiles in physical space are presented at different times: baseline condition.

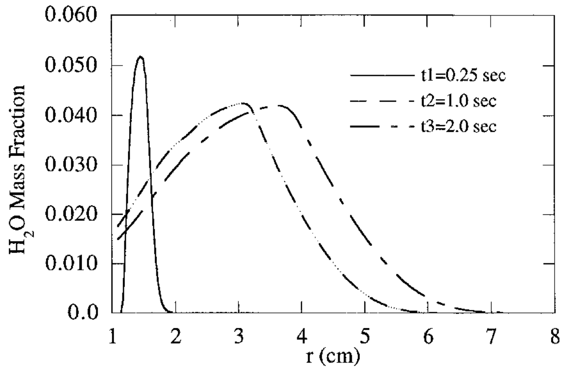

Fig. 7 Calculated H_2O species profiles in physical space are presented at different times: baseline condition.

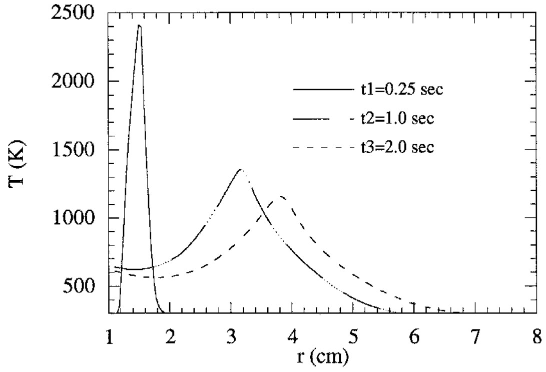

Fig. 8 Calculated temperature profiles are presented in physical space at different times: baseline condition.

ical space, and the radiation loss fraction reaches values in excess of 90% of the heat release rate as shown in Fig. 9.

The global features of the experimentally measured temperature profiles are also reasonably well predicted. As an example, two experimentally measured temperatures are compared with the calculated temperatures and presented in Fig. 10. The porous burner surface temperature distribution is predicted within 10% of the experimental data. An experimentally measured temperature at $r = 2.3$ cm from the burner center is predicted within 17% of the experimental data with uncertainties in the proper computational assumptions limiting this prediction (e.g., it is not known if the temperature measurements were radiation compensated, etc.).

Flow rate effects are shown in Fig. 11, where the total soot mass vs time is presented for three different fuel mass flow rates (20, 30, and 40 cm^3/s). As the fuel flow rate increases, the total soot mass increases, except at earliest times ($t < 0.1$ s), when total soot mass is essentially independent of fuel mass flow rate; the fuel concentration is sufficiently large everywhere. The dependence of the soot mass fraction on the flow rate is believed to result from the increased fuel mass fraction adjacent to the burner at increased flow rates. At higher flow rates, the local fuel mass fraction is increased, and given that the soot growth processes are roughly linear in the fuel mass fraction, it is not surprising to see increased soot mass at these relatively high flow rate conditions. The fuel mass fraction profiles on the spherical surfaces are presented in Fig. 12 for these three flow rates. As a theoretical observation, it is noted in Fig. 12 that the common boundary condition specification of fuel mass fraction equaling one at the burner would produce errors in the prediction of the surface mass fraction. Only at very early times for the lowest flow rate considered is the fuel mass fraction equal to unity at the burner surface. Obviously, with increased flow rates, the mass transfer Peclet number would increase to a point where the assumption would always be valid. For all of the flow rates considered in this study,

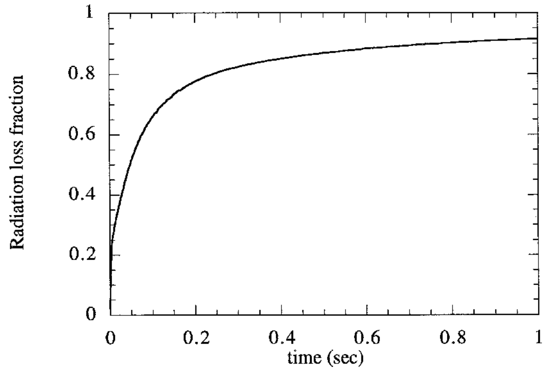

Fig. 9 Radiation loss fraction (defined as a ratio of the total radiative loss rate from the flame to the chemical heat release rate) is presented as a function of time: $\dot{V} = 20$ cc/s and $\varepsilon = 1$.

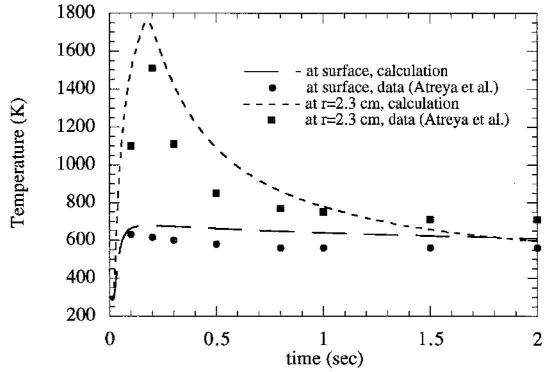

Fig. 10 Simulated temperatures at two locations are presented with experimentally measured temperatures as functions of time (baseline condition).

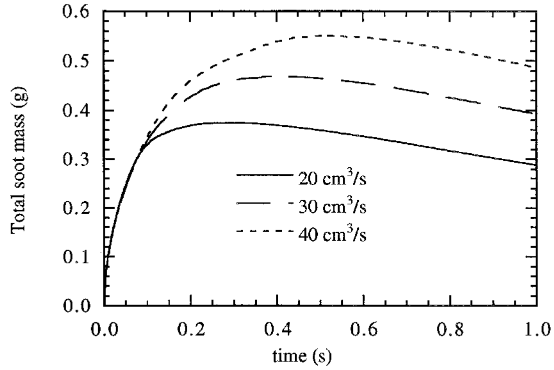

Fig. 11 Total soot mass is presented as a function of time for three flow rate conditions: $\varepsilon = 1$.

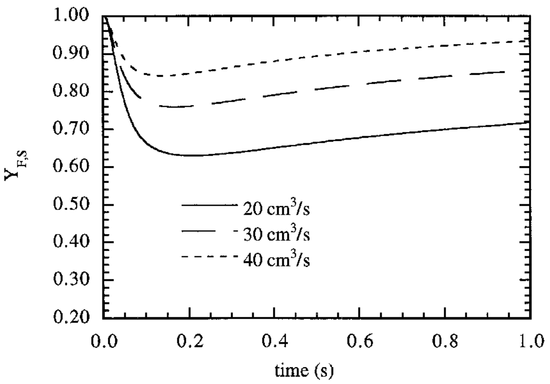

Fig. 12 Fuel mass fraction at the burner surface is presented as a function of time for three fuel flow rate values: ε = 1.

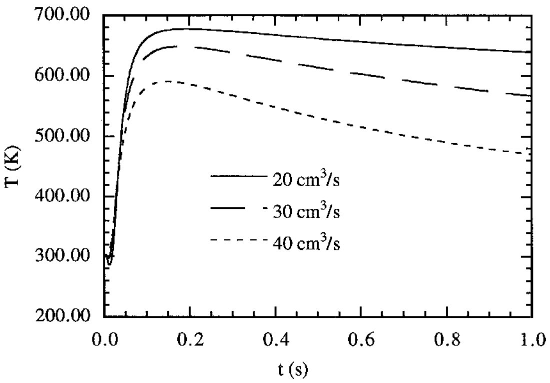

Fig. 13 Effects of fuel flow rate on the transient burner surface temperature are shown with burner emissivity equal to unity.

there are errors in such an approximation. Much in the same way that the surface fuel mass fraction is affected by the flow rate, the surface temperature dependence of flow rate is shown in Fig. 13. With varying flow rate, the surface temperature shows marked differences in character. At the lowest flow rate case, the surface temperature increases considerably during the transient ignition process and then establishes a quasi-steady-state value. For the highest flow rate condition, the surface temperature initially increases during the transient ignition process and then never appears to maintain a quasi-steady-state value. Instead, the surface temperature begins to decay to what may be a long-time quasisteady value. The decay for the high flow rate condition is caused by the relatively fast rate at which the reaction zone is blown away from the burner surface. As a result of the faster expanding flame, both diffusive and radiative heat flux interaction between the high temperature areas of the flame and the burner are reduced.

A physical parameter that significantly affects the heat transfer response of the flame-burner geometry is the burner emissivity. A range of values of the burner emissivity was used to clarify the radiative heat loss mechanism for this burner configuration. The radiant loss from the burner is shown in Fig. 14 for three representative values of the burner emissivity. While it is anticipated that the absolute magnitudes of the radiative heat flux would increase with increasing emissivity, it is somewhat less obvious that the radiant flux would be directed away from the burner. Figure 15 shows the burner surface temperature as a function of time for the three emissivity cases considered. Decreasing the burner emissivity is shown to increase the burner surface temperature, implying that the burner is radiatively cooled and conductively heated. A simple energy balance for a nominal flow rate value (e.g., 20 cc/s) establishes that conduction from the flame sheet to the burner raises the inlet fuel temperature from 300 K to the surface temperature 600 K and is redistributed as radiative heat transfer. There are interesting implications for this energy redistribution process. It is known that in large fires radiative transfer from the soot and fire products toward the fuel base maintains the fire. For such conditions, it would be desirable to have a low emissivity/absorptivity surface. On the other hand, for small-scale fires, both convective and conductive processes serve to heat and vaporize the fuel surface. From the effects that are shown in Figs. 14 and 15 it appears that radiative transfer for some small flames acts to decrease the rate of burning of the material in question. Based upon the scale of the flame/fire, the heat transfer mechanisms are modified.

Interestingly, the surface radiative flux does not significantly modify the soot mass produced by the flame. The soot mass profiles for the three emissivity cases are shown in Fig. 16. Soot mass is shown to be relatively insensitive to the burner temperature and emissivity. Somewhat larger amounts of soot are produced with increasing surface temperature.

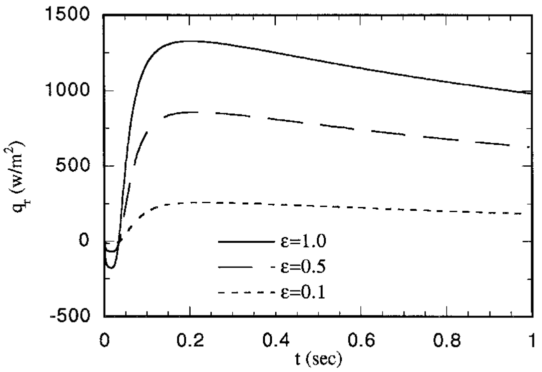

Fig. 14 Net radiative heat flux at the burner surface is presented as a function of time for three values of the burner emissivity: $\dot{V}$ = 20 cc/s.

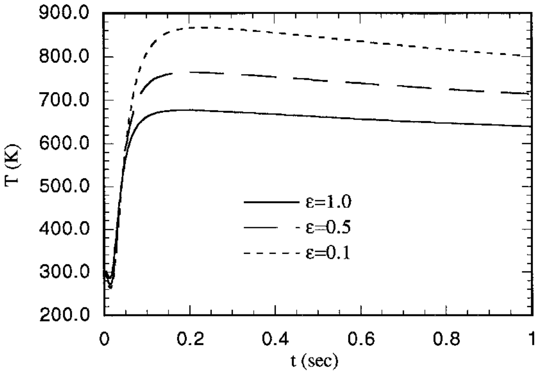

Fig. 15 Effects of burner emissivity on the transient burner surface temperature are shown. Fuel flow rate is 20 cc/s.

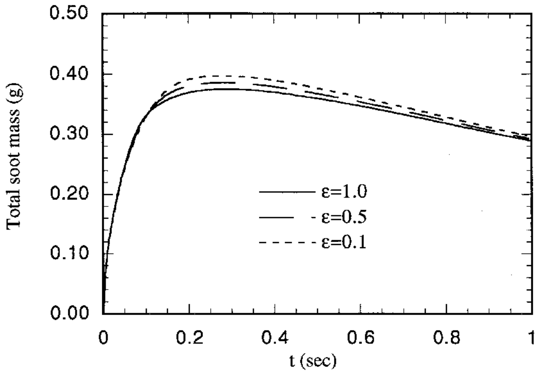

Fig. 16 Total soot mass variation with time is shown for three values of the burner emissivity with a fuel flow rate of 20 cc/s.

Conclusions

The global features of a microgravity counterflow diffusion flame were simulated using a numerical model that incorporated the fundamental submodels for a sooting flame. Both gas phase and soot chemical kinetics were modeled using rates available in the literature. Radiation was modeled with a spherical harmonics (P1 approximation) method using individual species Planck mean absorption coefficients. An effect of residence time is shown on the magnitude of the gas Planck mean absorption coefficient as compared to the soot mean absorption coefficient. The accumulation of unburned fuel and product gases at elevated temperatures increases the total radiative heat transfer rate for these flames. The predictions show good agreement with experimental results.

In these microgravity diffusion flames, the increased product accumulation enhances radiative transfer to a point where approximately 90% of the instantaneous heat release is lost radiatively. This was shown to significantly weaken the flame and later reduce the rate of production of soot species.

A significant effect was found in the flame properties as the fuel flow rate was changed. It was found that the effect of increasing fuel flow rate was to increase the local fuel concentration near the burner and subsequently increase the amount of soot formed in the system. Additionally, the increased flow rate was shown to reduce the burner surface temperature.

The burner emissivity was shown to significantly affect the radiative heat flux from the burner. For the relatively small flames that were considered, the primary heat transfer mechanism to the burner was conductive/convective. Radiative transfer was found to be a cooling mechanism for the burner. The burner heat transfer characteristics were not found to significantly affect the flame internal dynamics.

Acknowledgment

This work is supported by the National Institute of Standards and Technology under Grant 60NANB3D1436.

References

[1] Moss, B. J., Stewart, C. D., and Syed, K. J., "Flowfield Modeling of Soot Formation at Elevated Pressure," *22nd Symposium (International) on Combustion*, The Combustion Inst., Pittsburgh, PA, 1988, pp. 413–423.

[2] Kennedy, I. M., Kollmann, W., and Chen, J. Y., "A Model for Soot Formation in a Laminar Diffusion Flame," *Combustion and Flame*, Vol. 81, 1990, pp. 73–85.

[3] Makel, D. B., and Kennedy, I. M., "Soot Formation in Laminar Inverse Diffusion Flames," *Combustion Science and Technology*, Vol. 97, 1994, pp. 303–314.

[4] Syed, K. J., Stewart, C. D., and Moss, J. B., "Modeling Soot Formation and Thermal Radiation in Buoyant Turbulent Diffusion Flames," *23rd Symposium (International) on Combustion*, The Combustion Inst., Pittsburgh, PA, 1990, pp. 1533–1541.

[5] Kent, J. H., Jander, H., and Wagner, H. G., "Soot Formation in a Laminar Diffusion Flame," *18th Symposium (International) on Combustion*, The Combustion Inst., Pittsburgh, PA, 1981, pp. 1117–1125.

[6] Leung, K. M., Lindstedt, R. P., and Jones, W. P., "A Simplified Reaction Mechanism for Soot Formation in Nonpremixed Flames," *Combustion and Flame*, Vol. 87, 1991, pp. 289–305.

[7] Sivathanu, Y. R., and Gore, J. P., "Coupled Radiation and Soot Kinetics Calculations in Laminar Acetylene/Air Diffusion Flames," *Combustion and Flame*, Vol. 97, 1994, pp. 161–172.

[8] Ezekoye, O. A., and Zhang, Z., "Soot Oxidation and Agglomeration Modeling in a Microgravity Diffusion Flame," *Combustion and Flame* (to be published).

[9] Atreya, A., Agrawal, S., Shamim, T., Pickett, K., Sacksteder, K. R., and Baum, H. R., "Radiant Extinction of Gaseous Diffusion Flames," NASA Microgravity Workshop, Cleveland, OH, 1995.

[10] Fairweather, M., Jones, W. P., and Lindstedt, R. P., "Predictions of Radiative Transfer from a Turbulent Reacting Jet in a Cross-Wind," *Combustion and Flame*, Vol. 89, 1992, pp. 45–63.

[11] Modest, M. F., *Radiative Heat Transfer*, McGraw–Hill, New York, 1993, Chap. 14.

[12] Friedlander, S. K., *Smoke Dust and Haze*, Wiley, New York, 1977, Chap. 2.

[13] Kee, R. J., Rupley, F. M., and Miller, J. A., "Chemkin-II: A Fortran Chemical Kinetics Package for the Analysis of Gas-Phase Chemical Kinetics," Sandia National Lab., SAND89-8009, 1991.

[14] Kee, R. J., Dixon-Lewis, G., Warnatz, J., Coltrin, M. E., and Miller, J. A., "A Fortran Computer Code Package for the Evaluation of Gas-Phase Multicomponent Transport Properties," Sandia National Lab., SAND86-8246, 1991.

[15] Talbot, L., Cheng, R. K., Schefer, R. W., and Willis, D. R., *Journal of Fluid Mechanics*, Vol. 101, 1980, pp. 737–758.

[16] Skinner, S. M., "Flame Structure and Radiation Properties of Fuel Mixtures," M.S. Thesis, Univ. of Maryland, College Park, MD, 1990.

[17] Gore, J. P., and Skinner, M., "Mixing Rules for State Relationships of Methane and Acetylene/Air Diffusion Flames," *Combustion and Flame*, Vol. 87, 1991, pp. 357–364.

[18] Kuo, K., *Principles of Combustion*, Wiley, New York, 1986, Chap. 8.

[19] Westbrook, C. K., and Dryer, F. L., "Simplified Reaction Mechanisms for the Oxidation of Hydrocarbon Fuels in Flames," *Combustion Science and Technology*, Vol. 27, 1981, pp. 31–34.

[20] Siegel, R., and Howell, J. R., *Thermal Radiation Heat Transfer*, Hemisphere, New York, 1981, Chap. 17.

[21] Peters, N., "Laminar Diffusion Flamelet Models in Non-Premixed Turbulent Combustion," *Combustion Science and Technology*, Vol. 10, 1984, pp. 319–339.

[22] Chan, S. H., Pan, X. C., and Abou-Ellail, M., "Flamelet Structure of Radiating CH_4-Air Flames," *Combustion and Flame*, Vol. 102, 1995, pp. 438–446.